

Decoupled interband pairing in a bilayer iron-based superconductor evidenced by ultrahigh-resolution ARPES

Shichong Wang,^{1,2} Yuanyuan Yang,¹ Yang Li,^{2,3} Wenshan Hong,² Huaxun Li,⁴ Shaofeng Duan,^{2,1} Lingxiao Gu,^{1,2} Haoran Liu,^{1,2} Jiongyu Huang,^{1,2} Jianzhe Liu,^{1,2} Dong Qian,^{1,5,6} Guanghan Cao,^{4,5} Huiqian Luo,² and Wentao Zhang^{2,1,*}

¹*Key Laboratory of Artificial Structures and Quantum Control (Ministry of Education),
School of Physics and Astronomy, Shanghai Jiao Tong University, Shanghai 200240, China*

²*Beijing National Laboratory for Condensed Matter Physics,*

Institute of Physics, Chinese Academy of Sciences, Beijing 100190, China

³*School of Physical Sciences, University of Chinese Academy of Sciences, Beijing 100190, China*

⁴*School of Physics, Zhejiang University, Hangzhou 310058, China*

⁵*Collaborative Innovation Center of Advanced Microstructures, Nanjing University, Nanjing 210093, China*

⁶*Tsung-Dao Lee Institute, Shanghai Jiao Tong University, Shanghai 200240, China*

(Dated: January 13, 2026)

We present direct experimental evidence of a weakly coupled multiband superconducting state in the bilayer iron-based superconductor $\text{ACa}_2\text{Fe}_4\text{As}_4\text{F}_2$ ($\text{A} = \text{K}, \text{Cs}$) via ultrahigh-resolution angle-resolved photoemission spectroscopy (ARPES). Remarkably, the K -containing compound exhibits two distinct transition temperatures, corresponding to two separate sets of bilayer-split bands, as evidenced by temperature-dependent superconducting gap and spectral weight near the Fermi energy, while its Cs counterpart displays conventional single transition behavior. These experimental observations are well described by the weakly coupled two-band model of Eilenberger theory, which identifies suppressed interband pairing interactions between the bilayer-split bands as the key mechanism. By exploring quantum phenomena in the weak-coupling limit within a multiband system, our findings pave the way for engineering exotic superconductivity via band-selective pairing control.

The concept of multiband superconductivity, initially proposed through theoretical extensions of BCS theory to multiple electronic bands [1, 2], has undergone profound evolution driven by experimental discoveries. Early multiband systems like V_3Si [3], CeCu_2Si_2 [4], NbSe_3 [5], and Sr_2RuO_4 [6] provided intriguing research platforms but failed to fully establish the modern paradigm of multiband superconductivity. A pivotal advancement emerged with MgB_2 , where spectroscopic techniques unambiguously resolved two distinct superconducting gaps associated with σ - and π -bands [7–10]. This breakthrough propelled theoretical frameworks exploring interband coupling mechanisms, revealing that phonon-mediated interactions between bands could cooperatively enhance the critical temperature (T_c) [11–15]. Later studies established interband scattering—mediated by phonons, spin fluctuations, or other bosonic modes—as a critical determinant of superconducting phenomenology. This mechanism governs gap symmetry, T_c enhancement, and anomalous behaviors in thermodynamic responses [11, 16, 17]. A central question in multiband superconductivity involves reconciling the coexistence of strong interband coupling (as in MgB_2) and weakly coupled regimes exhibiting gap decoupling, for which no unambiguous cases have been confirmed. Although measurements of London penetration depth in V_3Si [18] and 2H-NbSe_2 [19] provide indirect evidence of weakly coupled gaps, direct spectroscopic validation through angle-resolved photoemission or quasiparticle interference remains undetected. Identifying materials with weak interband pairing is critical to distinguish universal multiband behavior from material-specific coupling effects.

Iron-based superconductors, discovered in 2008 [20], have emerged as a paradigmatic platform for multi-band superconductivity. The iron-based superconductors $\text{ACa}_2\text{Fe}_4\text{As}_4\text{F}_2$ ($\text{A} = \text{K}, \text{Rb}, \text{Cs}$; referred to as 12442) have emerged as structural analogs to bilayer cuprates, attracting significant attention due to their unique layered architecture, which features alternating double FeAs superconducting layers separated by insulating Ca_2F_2 blocks [21, 22]. The layered configuration induces bilayer splitting, resulting in two distinct sets of Fermi surfaces centered at the Γ point [23]. Despite extensive experimental investigations of the 12442 systems, some controversies remain in the experimental observations. A nodal gap has been suggested by muon-spin rotation (μSR) and point-contact Andreev-reflection spectroscopy studies [24–26], whereas transport, optical, scanning tunneling microscope (STM), and angle-resolved photoemission spectroscopy (ARPES) experiments have demonstrated that 12442 exhibits a nodeless gap [23, 27–30]. Additionally, optical experiments have provided indications of a pseudogap [31, 32].

Here, we present spectroscopic evidence of weak pairing scattering in the bilayer iron-based superconductor $\text{ACa}_2\text{Fe}_4\text{As}_4\text{F}_2$ utilizing ultrahigh-resolution ARPES. Specifically, with improved resolution, we observe distinct superconducting gaps in K12442 with two sets of transition temperatures ($T_c = 33.5$ K, $T_c^* \approx 22$ K) in the bilayer-split bands, indicating weak interband coupling. In contrast, the Cs -containing sample Cs12442 exhibits a single transition at the bulk $T_c = 30$ K, consistent with strong interband coupling. The aforementioned observations can be effectively explained by the different coupling strengths in the two-band model of Eliashberg theory. Furthermore, our high-resolution data reveal definitive evidence of nodeless superconducting gaps and establish the absence of pseudogap behavior near the Brillouin zone center.

* wentaozhang@iphy.ac.cn

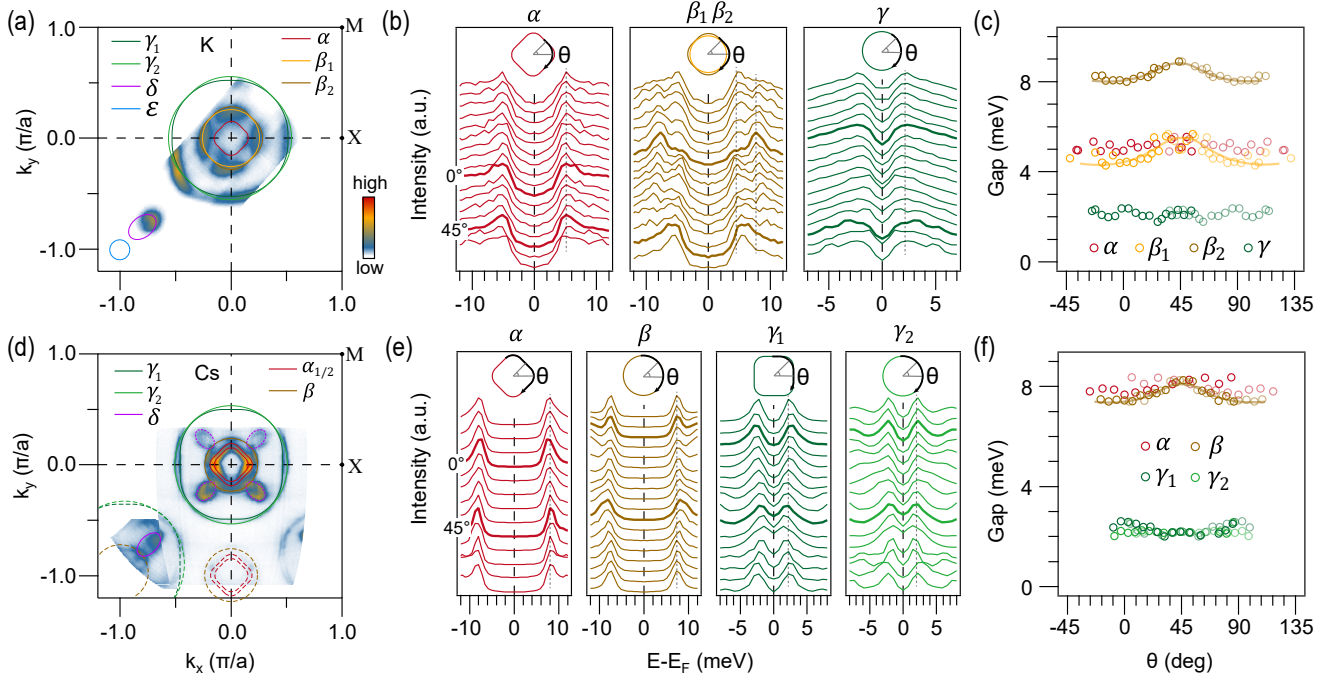


FIG. 1. Fermi surface topology and superconducting gap characteristics of K12442 (upper panel) and Cs12442 (lower panel) measured at 4 K. (a) Photoemission contour for K12442 at a binding energy of 10 meV. (b) Momentum-dependent symmetrized EDCs corresponding to the hole bands at the Γ point for K12442, with original EDCs shown in Supplemental Figs. S1 (b), (e) [33]. (c) Extracted energy gap size as a function of the marked angle shown in (b). The light hollow circles represent symmetrized data at $\theta = 45^\circ$ to highlight the symmetry. (d)–(f) Corresponding measurements on Cs12442. Dashed lines of various colors indicate the corresponding folded bands.

Low-temperature ultrahigh-resolution ARPES measurements at 4 K confirm that bilayer splitting is a common characteristic in the 12442 system (see methods in Supplemental Material [33]; see also Refs. [21, 34–39] therein). In K12442, the Fermi surface consists of three hole-like pockets at the Γ point: the α and β bands (primarily from d_{xz}/d_{yz} orbitals) and the γ band (primarily from d_{xy}). A small electron-like ε pocket is observed near M, surrounded by hole-like δ bands below the Fermi level [Fig. 1(a)] [23]. Pronounced splitting occurs along Γ -X, with minimal splitting along Γ -M [Fig. 2(a) and Supplemental Fig. S1(c) [33]]. Symmetrized energy distribution curves (EDCs) clearly resolve distinct energy gaps for the split β bands: $\Delta_{\beta_1} \sim 4.5$ meV (bonding) and $\Delta_{\beta_2} \sim 8.4$ meV (antibonding), along with $\Delta_\alpha \sim 5.0$ meV and $\Delta_\gamma \sim 2$ meV [Figs. 1(b) and (c)]. In Cs12442, band splitting is sharper [Fig. 1(d)] [40], with clearer surface reconstruction-induced folding effects (Supplemental Fig. S1(f) [33]). The α and γ bands exhibit more pronounced splitting than in the K-based compound, which is a consequence of stronger interlayer hopping and reduced inelastic scattering, with gap values of $\Delta_{\alpha 1} \sim \Delta_{\alpha 2} \sim 8.0$ meV ($\Delta_{\alpha 1}$: bonding band, $\Delta_{\alpha 2}$: antibonding band), $\Delta_{\gamma_1} \sim \Delta_{\gamma_2} \sim 2$ meV, forming two sets of hole pockets [Fig. 1(e)]. Despite these differences, both systems exhibit nearly isotropic superconducting gaps at the Γ point across all bands except the β band, which has a gap maximum along the zone diagonal [Figs. 1(c) and (f)]. No nodal gap is detected in the hole pockets near Γ in either K12442 or Cs12442.

Figure 2 reveals a stark contrast in the superconducting transitions of two samples. For K12442, data along the Γ -X direction show a dual-transition behavior. Symmetrized EDCs indicate the superconducting gap on the α and β_1 bands closes at a suppressed temperature ($T_c^* \sim 22$ K), well below the bulk T_c of 33.5 K, while the β_2 and γ bands close at T_c [Fig. 2(d), Supplemental Fig. S3 and Discussion III for validation of the symmetrization [33]]. This is confirmed by BCS gap fitting (Supplemental Discussion IV [33]), which identifies two distinct transitions [Fig. 2(b)]. The density of states (DOS) also shows two critical temperatures [Fig. 2(c)], with the lower one slightly suppressed versus the gap-derived T_c^* , suggesting a subtle decoupling between spectral coherence and gap formation. A small discrepancy in the exact T_c^* value between fitting methods indicates a residual gap persists above 22 K. This dual-transition phenomenon is robust across samples and thermal cycles (Supplemental Fig. S5) and is evidenced to be a bulk effect (Supplemental Discussion II; see also Refs. [29, 41, 42] therein) [33]. In sharp contrast, the Cs12442 sample exhibits a single, conventional BCS-like gap evolution at T_c for all bands [Figs. 2(e)–(h)]. The absence of this dichotomy in Cs12442 highlights the unique role of suppressed interband coupling in K12442, likely tied to its distinct bilayer splitting. No pseudogap signatures were observed near the Γ point in either compound (Supplemental Discussion III and Fig. S4 [33]).

In addition, we identified the electron-type ε band crossing the Fermi level and the δ band situated approximately 20

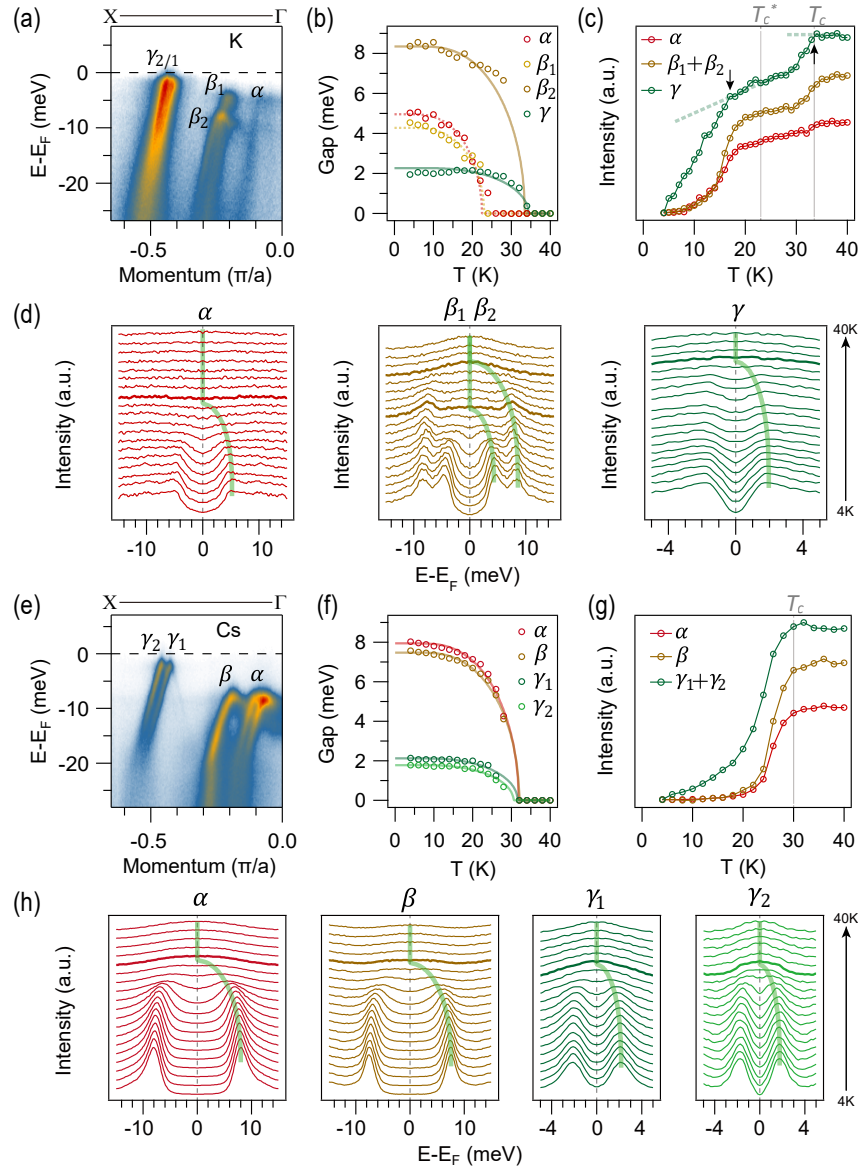


FIG. 2. Temperature-dependent measurements along Γ -X in K12442 (a–d) and Cs12442 (e–h). (a), (e) High resolution photoemission spectra acquired near the Fermi energy at 4 K. (d), (h) Symmetrized EDCs for the hole bands near the Γ point from 4 K to 40 K. Green guide lines highlight the temperature evolution of the superconducting gap. The determination of k_F for the β band is discussed in Supplemental Discussion III, and the original EDCs are shown in Supplemental Fig. S2 [33]. (b), (f) Temperature dependence of the extracted energy gaps from panels (d) and (h), respectively. Solid and dashed curves represent fits to the BCS gap function. (c), (g) Temperature-dependent intensity integrated within ± 0.5 meV of the Fermi energy for individual bands.

meV below the Fermi level [Fig. 3(a)]. At temperatures well below T_c , the ε band exhibits a nearly flat dispersion, with a superconducting energy gap of around 4.4 meV [Figs. 3(b) and (c)]. Consistent with the behavior observed in the α and β_1 bands, the temperature dependence of both the energy gap and spectral weight of the ε band reveals a distinct transition at a lower temperature, T_c^* . Notably, the spectral weight intensity also shows a subtle transition at T_c , similar to the α band. The consistent observation of dual transitions near the M point provides additional evidence for weak interband coupling in this multiband superconductor.

We employ a simplified two-band weak-coupling model

based on Eilenberger theory to interpret the experimental results [43]. This approach has previously demonstrated consistency with experimental measurements of superfluid density and heat capacity in multiband superconductors such as MgB_2 and V_3Si [43, 44]. In the two-band model, the energy gap equation $\Delta(T)$ can be numerically solved using the following equations (Supplemental Discussion V [33]; see also

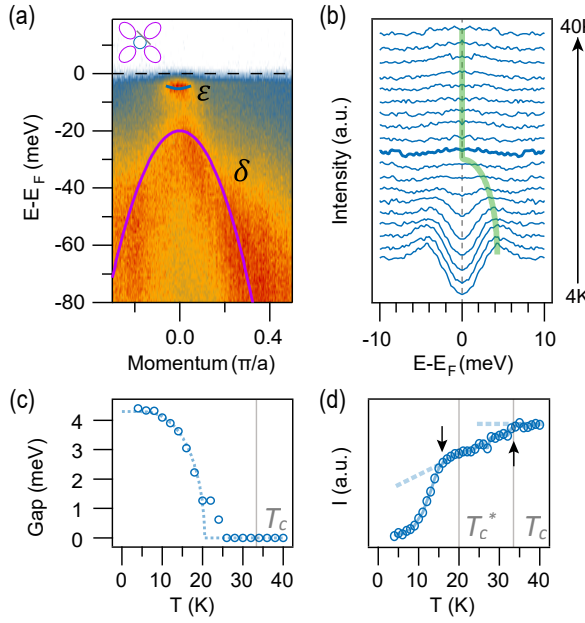


FIG. 3. Measurements on K12442 near the M point. (a) Photoemission spectrum at 4 K for the momentum cut illustrated in the inset. The dispersions of the ε and δ bands are schematized by the solid line. (b) Temperature-dependent symmetrized EDCs for the ε band (bolded at T_c^*). (c) Temperature dependence of the superconducting gap in the ε band fitted with a BCS function (dashed line). (d) Spectral weight intensity of the ε band within ± 0.5 meV of the Fermi level as a function of temperature.

[43–46] therein):

$$\Delta_\nu = \sum_{\mu=1,2} \lambda_{\nu\mu} \Delta_\mu [S + \ln(T/T_c) - \sum_{m=0}^{\infty} \left(\frac{1}{m+1/2} - \frac{1}{\sqrt{(\frac{\Delta_\nu}{2\pi T})^2 + (m+1/2)^2}} \right)]. \quad (1)$$

Here, $\nu = 1, 2$ represents the band index. The parameter S is calculated using the coupling strength determined by T_c (Supplemental Eqs. S10 and S12 [33]). The DOS for the two bands, n_1 and n_2 , satisfying $n_1 + n_2 = 1$, and the coupling strength $\lambda_{\nu\mu}$ is proportional to n_μ . Typically, the interband coupling is significantly weaker than the intraband coupling ($\lambda_{12}, \lambda_{21} \ll \lambda_{11}, \lambda_{22}$). The temperature dependence of the energy gaps in the two-band system can be numerically solved within the framework of Eilenberger theory using Eq. 1.

Numerical solutions for the energy gap are shown in Fig. 4 for weak, intermediate, and strong coupling. For the bilayer-split two bands, it is reasonable to assume $n_1 = n_2$, giving $\lambda_{12} = \lambda_{21}$. The strong coupling scenario exhibits excellent agreement with experimental observations in Cs12442, consistent with prior ARPES studies on MgB₂ [10]. Conversely, the results for K12442 are consistent with weak coupling, indicating that replacing Cs with K reduces the interlayer coupling. A key observation is that even a minimal interband coupling strength ($\lambda_{12} = \lambda_{21} = 0.001$) is sufficient to suppress the emergence of a secondary transition temperature, unless the bands are entirely decoupled ($\lambda_{12} = \lambda_{21} = 0$). Conse-

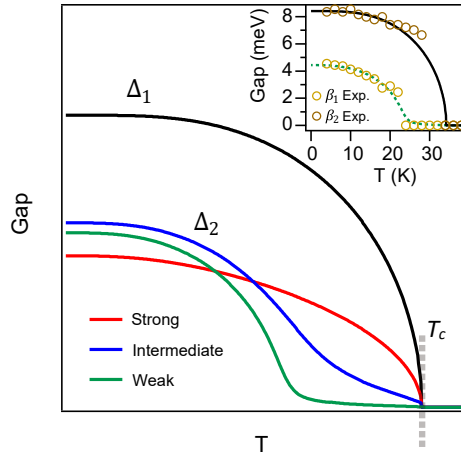


FIG. 4. Simulated energy gaps as a function of temperature based on the Eilenberger two-band model for varying interband coupling strengths. The interband coupling coefficients are defined as follows: weak coupling ($\lambda_{12} = \lambda_{21} = 0.001$), intermediate coupling ($\lambda_{12} = \lambda_{21} = 0.01$), and strong coupling ($\lambda_{12} = \lambda_{21} = 0.1$). The remaining parameters are fixed at $n_1 = n_2 = 0.5$, $\lambda_{11} = 1$, and $\lambda_{22} = 0.9$. A detailed discussion of the simulation methodology and results is provided in the Supplemental Discussion V [33]. The inset shows the temperature-dependent gaps for the bilayer-split bands β_1 and β_2 in K12442 under weak interband coupling.

quently, in the weak coupling regime, the partial energy gap does not fully close prior to T_c , leaving a tiny residual gap between T_c^* and T_c . This residual gap may be experimentally unresolvable, as suggested by the data in the inset of Fig. 4.

Lastly, we discuss the key factor that dominates the K-containing sample, so different from that of the Cs counterpart. We attribute the potential for weak coupling in K12442 to an anomalous reduction in the interaction potential during the pairing process. The interaction parameter $\lambda_{\nu\mu}$, which characterizes the coupling between bands, is proportional to the DOS ($n_\mu N(0)$) and the interaction potential ($V_{\nu\mu}$), defined as $\lambda_{\nu\mu} = n_\mu N(0) V_{\nu\mu}$. For the two samples in the 12442 system, the DOS $n_\mu N(0)$ is comparable, as the Fermi surface mappings in Figs. 1(a) and 1(d) give similar Fermi surface sheets. As discussed previously, the coupling strength $\lambda_{\nu\mu}$ is governed primarily by the interaction potential $V_{\nu\mu}$, which comprises the intraband electron pairing potential and the interband scattering potential between paired electrons [2]. Based on the above experimental observations, we conclude that the interband interaction potential $V_{\nu\mu}$ in the K sample should be significantly smaller than in the Cs sample. We note that the photoemission spectra for K12442 are broader, indicating heavier impurity scatterings than those in Cs12442. Our observations match a theoretical proposal where interband impurity scattering drives weak repulsive pairing and similar dual transitions in the temperature-dependent energy gap [12, 47]. Therefore, we conclude that impurity scattering plays a key role in mediating the interband pairing scattering potential. Furthermore, the variation in interlayer spacing of the Fe₂As₂ layers, which is controlled by the size of

the alkali atoms, also modulates this potential. Both of these factors are therefore crucial in determining the interband coupling strength $V_{\nu\mu}$.

In summary, using ultrahigh-resolution ARPES, we identify weakly coupled interband superconducting pairing in K12442, characterized by two distinct transition temperatures, while Cs12442 exhibits a single transition, consistent with strong coupling. These results are well described by a two-band Eilenberger theory with varying interband coupling strengths. This discovery provides a platform for studying the crossover between coupled and decoupled multiband superconductivity, reshaping the understanding of high- T_c systems where multiband physics and correlations are intertwined. In addition, based on the experimental observation, we propose that reduced interband scattering protects against gap suppression, thereby enhancing superconductivity. Our studies open new avenues for exploring band-selective pairing and electronic correlations in unconventional superconductivity.

ACKNOWLEDGMENTS

W. T. Z. acknowledges support from the National Key R&D Program of China (Grants No. 2021YFA1401800 and No. 2021YFA1400202), the National Natural Science Founda-

tion of China (Grants No. 12141404 and No. 12525404), and the Natural Science Foundation of Shanghai (Grants No. 22ZR1479700 and No. 23XD1422200). S. F. D. acknowledges support from the National Natural Science Foundation of China (Grants No. 12304178 and No. 12574166). D. Q. acknowledges support from the National Key R&D Program of China (Grants No. 2022YFA1402400 and No. 2021YFA1400100) and the National Natural Science Foundation of China (Grant No. 12074248). H. Q. L. acknowledges support from the National Key R&D Program of China (Grants No. 2023YFA1406100 and 2018YFA0704200) and the National Natural Science Foundation of China (Grants No. 11822411 and No. 12274444). G. H. C. acknowledges support from the National Key R&D Program of China (Grants No. 2022YFA1403202 and 2023YFA1406101).

DATA AVAILABILITY

The data that support the findings of this article are not publicly available upon publication because it is not technically feasible, and/or the cost of preparing, depositing, and hosting the data would be prohibitive within the terms of this research project. The data are available from the authors upon reasonable request.

[1] A. J. Leggett, Number-phase fluctuations in two-band superconductors, *Prog. Theor. Exp. Phys.* **36**, 901 (1966).

[2] H. Suhl, B. T. Matthias, and L. R. Walker, Bardeen-Cooper-Schrieffer theory of superconductivity in the case of overlapping bands, *Phys. Rev. Lett.* **3**, 552 (1959).

[3] G. F. Hardy and J. K. Hulm, Superconducting silicides and germanides, *Phys. Rev.* **89**, 884 (1953).

[4] F. Steglich, J. Aarts, C. D. Bredl, W. Lieke, D. Meschede, W. Franz, and H. Schäfer, Superconductivity in the presence of strong Pauli paramagnetism: CeCu₂S₂, *Phys. Rev. Lett.* **43**, 1892 (1979).

[5] P. Monceau, J. Peyrard, J. Richard, and P. Molinié, Superconductivity of the linear trichalcogenide NbSe₃ under pressure, *Phys. Rev. Lett.* **39**, 161 (1977).

[6] Y. Maeno, H. Hashimoto, K. Yoshida, S. Nishizaki, T. Fujita, J. G. Bednorz, and F. Lichtenberg, Superconductivity in a layered perovskite without copper, *Nature* **372**, 532 (1994).

[7] J. Nagamatsu, N. Nakagawa, T. Muranaka, Y. Zenitani, and J. Akimitsu, Superconductivity at 39 K in magnesium diboride, *Nature* **410**, 63 (2001).

[8] M. Iavarone, G. Karapetrov, A. E. Koshelev, W. K. Kwok, G. W. Crabtree, D. G. Hinks, W. N. Kang, E.-M. Choi, H. J. Kim, H.-J. Kim, and S. I. Lee, Two-band superconductivity in MgB₂, *Phys. Rev. Lett.* **89**, 187002 (2002).

[9] S. Souma, Y. Machida, T. Sato, T. Takahashi, H. Matsui, S.-C. Wang, H. Ding, A. Kaminski, J. C. Campuzano, S. Sasaki, and K. Kadowaki, The origin of multiple superconducting gaps in MgB₂, *Nature* **423**, 65 (2003).

[10] D. Mou, R. Jiang, V. Taufour, S. L. Bud'ko, P. C. Canfield, and A. Kaminski, Momentum dependence of the superconducting gap and in-gap states in MgB₂ multiband superconductor, *Phys. Rev. B* **91**, 214519 (2015).

[11] F. Bouquet, R. A. Fisher, N. E. Phillips, D. G. Hinks, and J. D. Jorgensen, Specific heat of Mg¹¹B₂: Evidence for a second energy gap, *Phys. Rev. Lett.* **87**, 047001 (2001).

[12] A. Y. Liu, I. I. Mazin, and J. Kortus, Beyond Eliashberg superconductivity in MgB₂: Anharmonicity, two-phonon scattering, and multiple gaps, *Phys. Rev. Lett.* **87**, 087005 (2001).

[13] H. Choi, D. Roundy, H. Sun, M. Cohen, and S. Louie, The origin of the anomalous superconducting properties of MgB₂, *Nature* **418**, 758 (2002).

[14] M. Zehetmayer, H. W. Weber, and E. Schachinger, Separable model calculations for the anisotropic properties of MgB₂, *J. Low Temp. Phys.* **133**, 407 (2003).

[15] E. J. Nicol and J. P. Carbotte, Properties of the superconducting state in a two-band model, *Phys. Rev. B* **71**, 054501 (2005).

[16] A. V. Sologubenko, J. Jun, S. M. Kazakov, J. Karpinski, and H. R. Ott, Thermal conductivity of single-crystalline MgB₂, *Phys. Rev. B* **66**, 014504 (2002).

[17] M. Zehetmayer, M. Eisterer, J. Jun, S. M. Kazakov, J. Karpinski, and H. W. Weber, Magnetic field dependence of the reversible mixed-state properties of superconducting MgB₂ single crystals and the influence of artificial defects, *Phys. Rev. B* **70**, 214516 (2004).

[18] K. Cho, M. Kończykowski, S. Ghimire, M. A. Tanatar, L.-L. Wang, V. G. Kogan, and R. Prozorov, Multiband superconductivity in V₃Si determined from studying the response to controlled disorder, *Phys. Rev. B* **105**, 024506 (2022).

[19] A. Alshemi, E. M. Forgan, A. Hiess, R. Cubitt, J. S. White, K. Schmalzl, and E. Blackburn, Two characteristic contributions to the superconducting state of 2H-NbSe₂, *Phys. Rev. Lett.* **134**, 116001 (2025).

[20] Y. Kamihara, T. Watanabe, M. Hirano, and H. Hosono, Iron-based layered superconductor La[O_{1-x}F_x]FeAs ($x = 0.05 -$

Decoupled interband pairing in a bilayer iron-based superconductor evidenced by ultrahigh-resolution angle-resolved photoemission spectroscopy: Supplemental Material

Shichong Wang,^{1,2} Yuanyuan Yang,¹ Yang Li,^{2,3} Wenshan Hong,² Huaxun Li,⁴ Shaofeng Duan,^{2,1} Lingxiao Gu,^{1,2} Haoran Liu,^{1,2} Jiongyu Huang,^{1,2} Jianzhe Liu,^{1,2} Dong Qian,^{1,5,6} Guanghan Cao,^{4,5} Huiqian Luo,² and Wentao Zhang^{2,1,*}

¹*Key Laboratory of Artificial Structures and Quantum Control (Ministry of Education), School of Physics and Astronomy, Shanghai Jiao Tong University, Shanghai 200240, China*

²*Beijing National Laboratory for Condensed Matter Physics, Institute of Physics, Chinese Academy of Sciences, Beijing 100190, China*

³*School of Physical Sciences, University of Chinese Academy of Sciences, Beijing 100190, China*

⁴*School of Physics, Zhejiang University, Hangzhou 310058, China*

⁵*Collaborative Innovation Center of Advanced Microstructures, Nanjing University, Nanjing 210093, China*

⁶*Tsung-Dao Lee Institute, Shanghai Jiao Tong University, Shanghai 200240, China*

Abstract

This Supplemental Material includes five additional discussions, five additional figures, and one supplementary data table.

* wentaozhang@iphy.ac.cn

I. METHODS

High-quality single crystals of $\text{KCa}_2\text{Fe}_4\text{As}_4\text{F}_2$ and $\text{CsCa}_2\text{Fe}_4\text{As}_4\text{F}_2$ were synthesized via flux method [S1–4]. Bulk superconductivity was confirmed by transport measurements, revealing sharp transitions at $T_c = 33.5$ K (K12442) and 30 K (Cs12442). Ultrahigh-resolution ARPES was performed with a 7 eV vacuum ultraviolet laser featuring an amplified repetition rate of 2 GHz to minimize space charge effects. This setup achieved an exceptional energy resolution of 0.26 meV at high count rates [S5], thereby enabling the precise and efficient tracking of the temperature-dependent energy gap [S6]. The laser spot size on the sample is approximately 35 μm . The probe laser is operating at a repetition rate of 2 GHz to reduce the space charge effect while maintaining high photon flux. Samples were cleaved in situ under ultra-high vacuum ($< 3 \times 10^{-11}$ torr). During the temperature-dependent measurements, the beam spot on the sample was stabilized with an accuracy better than 1 μm using a sample-position auto correction system [S7]. Leveraging the low work function of approximately 3 eV in this sample, we utilized a 7 eV laser to achieve ultrahigh-resolution measurements of the electronic states near the M point in K12442.

II. CONCLUSIVE EXPERIMENTAL OBSERVATION

The observation of dual superconducting transitions is an intrinsic property of the bulk material, ruling out explanations based on surface termination heterogeneity or bulk-surface discrepancies. This conclusion is firmly supported by the following experimental evidence: (i) identical spectral features, including consistent multi-gap characteristics with gap sizes agreeing with prior studies [S8, 9], are observed across multiple cleaved surfaces (with STM-dominant termination [S8]); (ii) the clear resolution of two distinct Fermi surfaces, corresponding to bilayer-split bands from inter bilayer hopping within the double Fe_2As_2 layers, provides direct evidence of electronic splitting without mixed termination signals; (iii) analysis of the Fermi surface sizes of the β_1 and β_2 bands in K12442 further corroborates the bilayer splitting scenario, as the β_1 band—though possessing a smaller energy gap—does not exhibit the larger hole pocket expected from additional hole doping, which would occur if it were a surface state due to potassium loss; (iv) this interpretation is strengthened by contrasting these results with those from Cs12442, where, despite the greater tendency of Cs atoms to escape from the cleaved surface and potentially create multiple terminations [S10], all Cs samples exhibit only a single transition at $T_c = 30$ K with no evidence of a

surface-related transition at lower temperature.

III. EDCS ON THE FERMI SURFACE SHEETS

Accurate determination of the Fermi momentum (k_F) is a prerequisite for reliable energy gap extraction. As shown in Fig. S3(a), the spectrum divided by the Fermi-Dirac distribution clearly demonstrates the transition of the energy gap in K12442, allowing for the extraction of the Fermi momentum k_F from the Fermi crossing above T_c . We observe that the energy gaps of the α and β_1 bands are nearly closed between 14 K to 24 K, whereas those of the γ and the β_2 bands persist up to $T_c = 33.5$ K. This asynchronous gap closure provides direct evidence for two distinct critical temperatures within the split bands. Additionally, since the k_F values of the β_1 and β_2 bands show negligible difference above T_c , we omit separate EDC analyses for these bands in the main text.

Figures S3(a) and (c) display the temperature-dependent photoemission spectra of K12442 and Cs12442 divided by the Fermi-Dirac distribution (FD) function. Distinct Bogoliubov quasiparticle peaks are observed above the Fermi level (E_F), providing direct evidence of particle-hole symmetry. The EDCs of different bands, as discussed in main text, were selected to be divided by the Fermi-Dirac distribution function, and compared them with the symmetrized EDCs and raw data. To resolve the Bogoliubov peaks above E_F , the analysis focuses on temperatures slightly below T_c , as electrons occupy states above the Fermi level. The consistency between the FD-divided peaks and the symmetrized data confirms the particle-hole symmetry and validates the symmetrization procedure employed in the main text.

The absence of a pseudogap in the hole pockets near the Γ point was confirmed by temperature-dependent ARPES experiments above T_c . To further clarify this, we extracted the energy gap of the β band and the intensity near the Fermi level in K12442 above the superconducting transition temperature ($T_c = 33.5$ K). The symmetrized EDCs of the β band collapse into a single peak above T_c (Fig. S4(a)), indicating the complete closure of the energy gap. Furthermore, the spectral intensity remains nearly constant between 33.5 K and 70 K (Fig. S4(b)), showing no indication of a pseudogap. A similar behavior was observed for the other energy bands near the Γ point and in Cs samples, as detailed in Fig. 2 of the main text.

IV. BCS GAP FITTING PROCEDURE

To determine the superconducting transition temperature, we analyzed experimental temperature-dependent energy gap data through numerical fitting procedures grounded in the BCS self-consistent equation [S11]

$$G(\Delta) = \ln \frac{T}{T_c} + \pi k_B T \sum_{\epsilon_n} \left[\frac{1}{|\epsilon_n|} - \frac{1}{\sqrt{\epsilon_n^2 + \Delta^2}} \right], \quad (\text{S16})$$

by introducing $\epsilon_n = 2\pi k_B T(n - \frac{1}{2})$ (n is a positive integer), we obtain the numerical solution for the BCS energy gap as a function of temperature. The numerical calculation begins with an initial guess for superconducting transition temperature T_c and energy gap size $\Delta(0)$, and iterates to derive a temperature-dependent energy gap equation, continuing until the discrepancy between the calculated results and experimental data falls within an acceptable error. Such fitting procedure yields errors in T_c of less than 1.5 K, as shown in TABLE I. The fitted transition temperatures indicate a dual transition regime in K12442 but a single transition $T_c = T_{c,\text{bulk}} \sim 30$ K in Cs12442. For various bands in K12442, an earlier transition temperature $T_c^* \sim 22$ K is reasonably fitted from the temperature-dependent energy gap data for the α , β_1 and ε bands, whereas other bands follow the bulk transition at $T_c \sim 33.5$ K, demonstrating consistency with Figs. 2 and 3 in the main text.

V. NUMERICAL SIMULATION OF TWO-BAND MODEL

A two-band weak-coupling model based on Eilenberger theory was employed to explain the bandgap transition phenomenon in multi-band superconductors [S12, 13]. Here, the formula and the numerical solution presented in the main text will be discussed in more detail.

Starting with the Eilenberger quasiclassical version of Gor'kov's theory [S14], a concise representation of the anisotropic Fermi surface is given by

$$\mathbf{v}\Pi f = 2\Delta g/\hbar - 2\omega f, \quad (\text{S1})$$

$$-\mathbf{v}\Pi^* f^+ = 2\Delta^* g/\hbar - 2\omega f^+, \quad (\text{S2})$$

$$g^2 = 1 - f f^+, \quad (\text{S3})$$

$$\Delta(\mathbf{r}, \mathbf{v}) = 2\pi T N(0) \sum_{\omega}^{\omega_D} \langle V(\mathbf{v}, \mathbf{v}') f(\mathbf{v}', \mathbf{r}, \omega) \rangle_{\mathbf{v}'} . \quad (\text{S4})$$

In these equations, $\Delta(\mathbf{r})$ is the gap function at \mathbf{k}_F values or different Fermi velocities \mathbf{v} . The operator Π is defined as $\nabla + 2\pi i \mathbf{A}/\phi_0$, where ϕ_0 is the flux quantum. The functions f , g , and f^+ correspond to the Eilenberger Green function. $N(0)$ denotes the density of states at the Fermi energy for each spin. $\omega = \omega_m$ represents the Matsubara frequencies, defined as $\hbar\omega = \pi T(2m+1)$, where m is a positive integer, and ω_D denotes the Debye frequency. The average intensity at the Fermi surface is defined as

$$\langle X \rangle = \int \frac{d^2\mathbf{k}_F}{(2\pi)^3 \hbar N(0) |\mathbf{v}|} X. \quad (\text{S5})$$

Considering the two-band model, the energy gap at different Fermi momentum \mathbf{k}_F can be written by

$$\Delta(k) = \Delta_{1,2}, \quad k \in F_{1,2}, \quad (\text{S6})$$

where F_1 and F_2 represent two sets of Fermi surface sheets. Since only two state densities N_1 and N_2 are considered, the average weight on each Fermi surface sheet is written by

$$\langle X \rangle = (X_1 N_1 + X_2 N_2)/N(0) = n_1 X_1 + n_2 X_2, \quad (\text{S7})$$

where $n_{1,2} = N_{1,2}/N(0)$ with $n_1 + n_2 = 1$. This analysis assumes the absence of electric and magnetic fields, implying that $\Pi = 0$. Under these conditions, the Eilenberger equations reduce to

$$f_\nu = \frac{\Delta_\nu}{\beta_\nu}, \quad g_\nu = \frac{\hbar\omega}{\beta_\nu}, \quad \beta_\nu^2 = \Delta_\nu^2 + \hbar^2\omega^2, \quad (\text{S8})$$

where $\nu = 1, 2$ represents the band index and β_ν depends on the position of the Fermi momentum \mathbf{k}_F .

In the above case, the energy gap equation Eq. (S4) for a simple two-band system can be written by

$$\Delta_\nu = 2\pi T \sum_{\mu=1,2} \lambda_{\nu\mu} f_\mu = \sum_{\mu} \lambda_{\nu\mu} \Delta_\mu \sum_{\omega} \frac{2\pi T}{\beta_\mu}, \quad (\text{S9})$$

where $\lambda_{\nu\mu}$ denotes the band interaction and should be proportional to the density of states, i.e., $\lambda_{\nu\mu} = n_\mu N(0) V_{\nu\mu}$. $V_{\nu\mu}$ represents the effective coupling potential in the two band system.

For the limit where $T \rightarrow T_c$, with $\Delta \rightarrow 0$ and $\beta \rightarrow \hbar\omega$. the summation term of Eq. (S9) gives

$$S = \sum_{\omega} \frac{2\pi T}{\hbar\omega} = \ln \frac{2\hbar\omega_D}{T_c \pi e^{-\gamma}} \approx \ln \frac{2\hbar\omega_D}{1.76 T_c}. \quad (\text{S10})$$

The constant $\pi e^{-\gamma} \approx 1.76$ (γ : Euler constant) is characteristic of BCS superconductors and is independent of the material.

By substituting S into Eq. (S9), the relationship between S and λ is obtained,

$$\Delta_1 = S(\lambda_{11}\Delta_1 + \lambda_{12}\Delta_2), \quad \Delta_2 = S(\lambda_{21}\Delta_1 + \lambda_{22}\Delta_2). \quad (\text{S11})$$

To ensure a non-trivial solution for this system of equations,

$$S = \frac{\lambda_{11} + \lambda_{22} - \sqrt{(\lambda_{11} - \lambda_{22})^2 + 4\lambda_{12}\lambda_{21}}}{2(\lambda_{11}\lambda_{22} - \lambda_{12}\lambda_{21})}. \quad (\text{S12})$$

For temperature far away from the T_c ,

$$S = \sum_{\omega}^{\omega_D} \frac{2\pi T}{\hbar\omega} + \ln \frac{T}{T_c}. \quad (\text{S13})$$

The temperature correction term, $\ln(T/T_c)$, can be calculated by converting the discrete summation involving the energy gap in Eq. (S9) into an integral form. In our numerical calculations, S was evaluated from Eq. (S12) for different coupling coefficients $\lambda_{\nu\mu}$. Now the Eq. (S9) is written as

$$\Delta_{\nu} = \sum_{\mu} \lambda_{\nu\mu} \Delta_{\mu} \left[\sum_{\omega}^{\infty} \left(\frac{2\pi T}{\beta_{\mu}} - \frac{2\pi T}{\hbar\omega} \right) + S - \ln \frac{T}{T_c} \right]. \quad (\text{S14})$$

By treating the Matsubara frequencies $\omega = \omega_m$ as integers, the equation of energy gap gives

$$\Delta_{\nu} = \sum_{\mu=1,2} \lambda_{\nu\mu} \Delta_{\mu} \left[\left(S + \ln \frac{T}{T_c} \right) - \sum_{m=0}^{\infty} \left(\frac{1}{m + 1/2} - \frac{1}{\sqrt{\left(\frac{\Delta_{\nu}}{2\pi T} \right)^2 + (m + 1/2)^2}} \right) \right]. \quad (\text{S15})$$

Building on the above equation and chosen coupling coefficients, iterative calculations yield the functional dependence of the energy gap Δ_{ν} on temperature T . In the numerically calculated results presented in Fig. 4 of the main text, the summation is truncated at 500 terms—a cutoff confirmed to sufficiently capture the temperature-dependent energy gap with convergence accuracy.

TABLE I. Summary of the transition temperatures T_c and zero-temperature energy gaps $\Delta(0)$ for all resolvable bands in K12442 and Cs12442. Values are derived from BCS fits to the temperature-dependent experimental data. Uncertainties in $\Delta(0)$ are estimated to be less than 0.1 meV.

	Band index	$\Delta(0)$ (meV)	T_c (K)
K12442	α	5.0	22.4 ± 0.4
	β_1	4.3	23.0 ± 0.8
	β_2	8.3	33.4 ± 1.4
	γ	2.3	34.4 ± 0.2
	ε	4.3	20.5 ± 0.1
Cs12442	α	7.9	31.9 ± 0.3
	β	7.3	31.8 ± 0.3
	γ_1	2.1	31.6 ± 0.9
	γ_2	1.8	30.5 ± 0.6

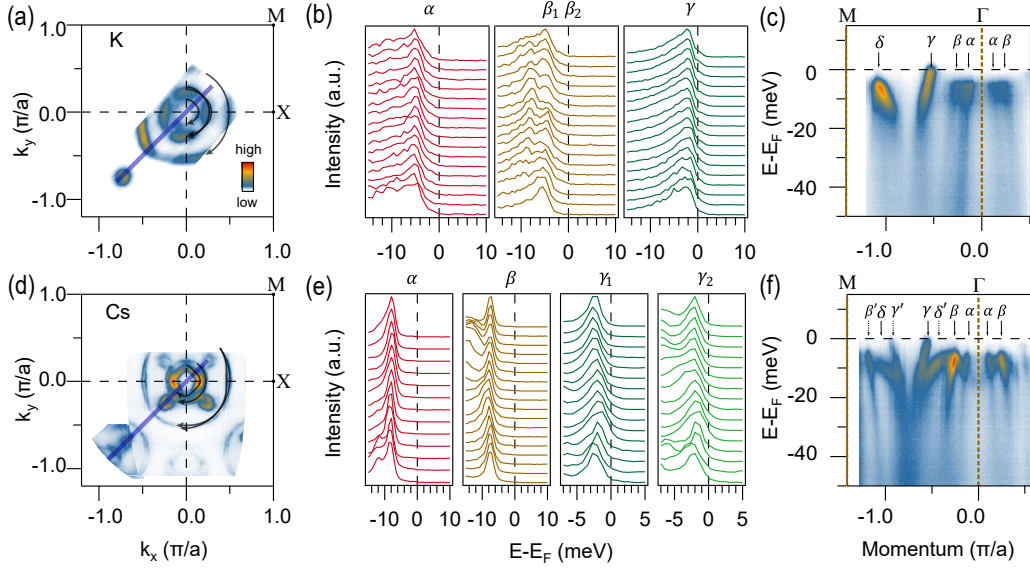


Fig. S1. Raw data for K12442 (upper panel) and Cs12442 (lower panel). (a) Photoemission contour for K12442 at a binding energy of 10 meV. The black arrows indicate the momentum measurement of different Fermi surface sheets, and the blue line denotes the cut direction from $\Gamma(0, 0)$ to $M(\pi, \pi)$. (b) Raw EDCs for Fig. 1(b) in the main text, showing the energy gap evolution along the different Fermi surface sheets of K12442. (c) Band structures along Γ -M in K12442, with the cut direction indicated by the blue solid line in (a). Black arrows denote different energy bands, and dashed arrows indicate folded bands. (d-f) Corresponding measurements for Cs12442.

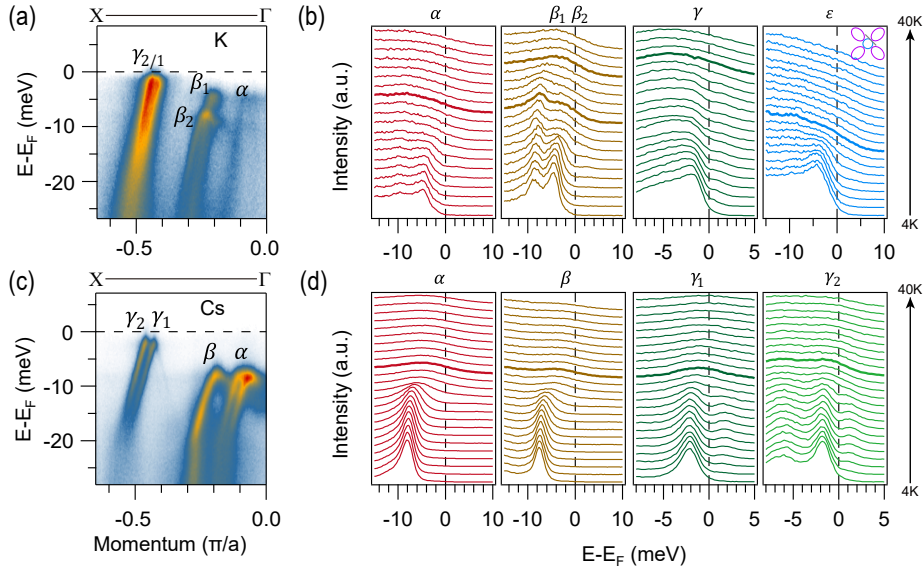


Fig. S2. Raw EDCs from temperature-dependent experiments of K12442 (upper panel) and Cs12442 (lower panel). (a) Photoemission spectrum of K12442 measured at 4 K, with band indices marked; the corresponding spectrum for Cs12442 is shown in (c). (b) Raw EDCs of K12442, corresponding to the symmetrized results in Figs. 2(d) and 3(b) of the main text. (d) Raw EDCs of Cs12442, corresponding to Fig. 2(h) of the main text (Cs12442). The bold lines in (b) and (d) indicate EDCs taken at the transition temperature..

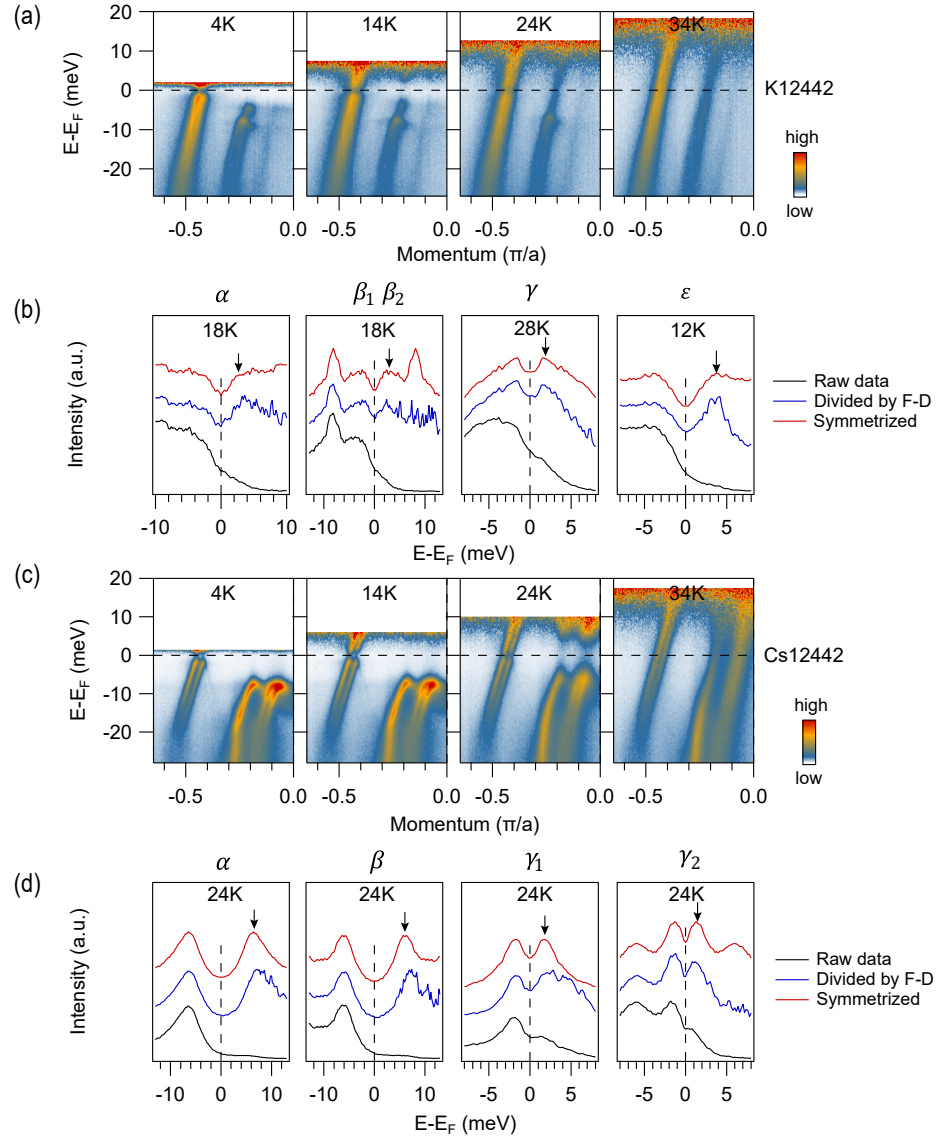


Fig. S3. Temperature-dependent photoemission spectrum and EDCs divided by the Fermi-Dirac distribution (FD) in K12442 and Cs12442. (a) FD-divided spectrum of K12442 measured at 4 K, 14 K, 24 K, and 34 K. (b) Comparison of the FD-divided EDCs (taken below T_c) with raw data and symmetrized EDCs. Black arrows indicate the Bogoliubov quasiparticle peaks. (c)-(d) Corresponding measurements for Cs12442.

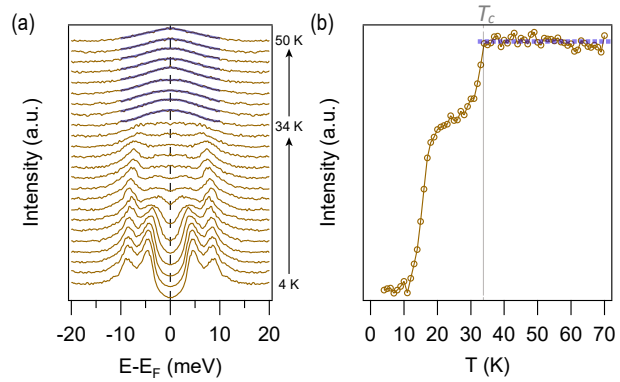


Fig. S4. Temperature evolution of the β band in K12442. (a) Symmetrized EDCs for the β band from 4 K to 50 K. Blue solid curves are fits to the data above above T_c . (b) Temperature-dependent intensity integrated near the Fermi energy for β band up to 70 K. The blue dashed line serves as a guideline indicating the intensity remains constant above T_c .

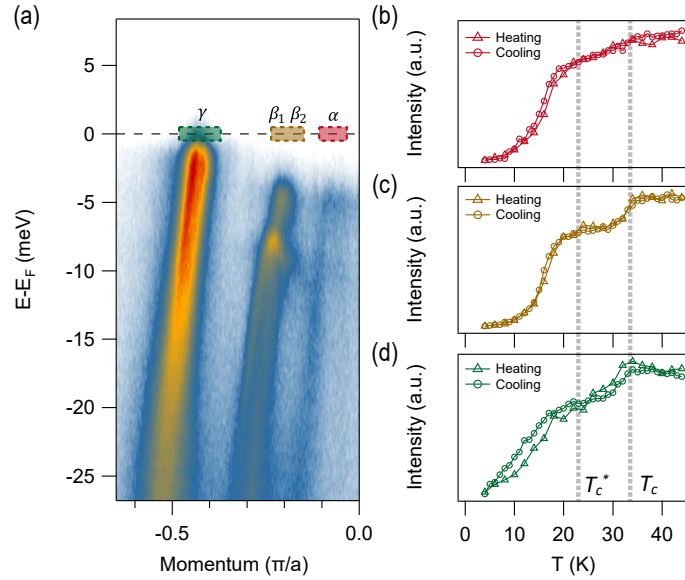


Fig. S5. Comparison between heating and cooling cycles in K12442. (a) Low-temperature photoemission spectrum. Colored markers indicate the momentum integration ranges for the three bands, with the energy range being $E_F \pm 0.5$ meV. (b)-(d) Temperature dependence of the spectral intensity for the α , β , γ bands, comparing heating and cooling measurements.

[S1] T. Wang, J. Chu, J. Feng, L. Wang, X. Xu, W. Li, H. Wen, X. Liu, and G. Mu, Low temperature specific heat of 12442-type $KCa_2Fe_4As_4F_2$ single crystals, *Sci. China Phys. Mech. Astron.* **63**, 297412 (2020).

[S2] Z.-C. Wang, C.-Y. He, S.-Q. Wu, Z.-T. Tang, Y. Liu, A. Ablimit, C.-M. Feng, and G.-H. Cao, Superconductivity in $KCa_2Fe_4As_4F_2$ with separate double Fe_2As_2 layers, *J. Am. Chem. Soc.* **138**, 7856 (2016).

[S3] D. T. Adroja, S. J. Blundell, F. Lang, H. Luo, Z.-C. Wang, and G.-H. Cao, Observation of a neutron spin resonance in the bilayered superconductor $CsCa_2Fe_4As_4F_2$, *J. Phys.: Condens. Matter* **32**, 435603 (2020).

[S4] W. Hong, L. Song, B. Liu, Z. Li, Z. Zeng, Y. Li, D. Wu, Q. Sui, T. Xie, S. Danilkin, H. Ghosh, A. Ghosh, J. Hu, L. Zhao, X. Zhou, X. Qiu, S. Li, and H. Luo, Neutron spin resonance in a quasi-two-dimensional iron-based superconductor, *Phys. Rev. Lett.* **125**, 117002 (2020).

[S5] C. Huang, S. Duan, and W. Zhang, High-resolution time- and angle-resolved photoemission studies on quantum materials, *Quantum Front.* **1**, 15 (2022).

[S6] Y. Yang, Q. Wang, S. Duan, H. Wo, C. Huang, S. Wang, L. Gu, D. Qian, J. Zhao, and W. Zhang, Unusual band splitting and superconducting gap evolution with sulfur substitution in $FeSe$, *Chin. Phys. Lett.* **39**, 057302 (2022).

[S7] S. Duan, S. Wang, Y. Yang, C. Huang, L. Gu, H. Liu, and W. Zhang, A sample-position-autocorrection system with precision better than $1\ \mu m$ in angle-resolved photoemission experiments, *Rev. Sci. Instrum.* **93**, 103905 (2022).

[S8] W. Duan, K. Chen, W. Hong, X. Chen, H. Yang, S. Li, H. Luo, and H.-H. Wen, Single-particle tunneling spectroscopy and superconducting gaps in the layered iron-based superconductor $KCa_2Fe_4As_4F_2$, *Phys. Rev. B* **103**, 214518 (2021).

[S9] S. Shao, F. Zhang, Z. Zhang, T. Wang, Y. Wu, Y. Tu, J. Hou, X. Hou, N. Hao, G. Mu, and L. Shan, Superconductivity and pseudogap features of an isolated $FeAs$ layer in $KCa_2Fe_4As_4F_2$ unraveled by stm/sts, *Sci. China Phys. Mech. Astron.* **66**, 287412 (2023).

[S10] H. Liu, S. Duan, X. Liu, Z. Liu, S. Wang, L. Gu, J. Huang, W. Yang, J. Liu, D. Qian, Y. Guo, and W. Zhang, Fluctuated lattice-driven charge density wave far above the condensation temperature in kagome superconductor KV_3Sb_5 , *Science Bulletin* **70**, 1211 (2025).

- [S11] J. Bardeen, L. N. Cooper, and J. R. Schrieffer, Theory of superconductivity, *Phys. Rev.* **108**, 1175 (1957).
- [S12] V. G. Kogan, C. Martin, and R. Prozorov, Superfluid density and specific heat within a self-consistent scheme for a two-band superconductor, *Phys. Rev. B* **80**, 014507 (2009).
- [S13] R. Prozorov and V. G. Kogan, London penetration depth in iron-based superconductors, *Rep. Prog. Phys.* **74**, 124505 (2011).
- [S14] G. Eilenberger, Transformation of Gorkov's equation for type II superconductors into transport-like equations, *Z. Physik* **214**, 195 (1968).